Advances in Geo-Energy Research

Vol. 12, No. 3, p. 205-222, 2024

Original article

Molecular simulations of the effects of CO_2 and N_2 injection on CH_4 adsorption, coal porosity and permeability

Jienan Pan[1]*, Fengmei Jiao[1], Kai Wang[1], Yunbo Li[1], Dangyu Song[1], Quanlin Hou[2]

[1]*School of Resources & Environment, Collaborative Innovation Center of Coalbed Methane and Shale Gas for Central Plains Economic Region, Henan Polytechnic University, Jiaozuo 454000, P. R. China*

[2]*Key Lab of Computational Geodynamics, College of Earth and Planetary Sciences, University of Chinese Academy of Sciences, Beijing 100049, P. R. China*

Keywords:
Molecular simulation
CO_2 injection
N_2 injection
CH_4 adsorption
permeability

Cited as:
Pan, J., Jiao, F., Wang, K., Li, Y., Song, D., Hou, Q. Molecular simulations of the effects of CO_2 and N_2 injection on CH_4 adsorption, coal porosity and permeability. Advances in Geo-Energy Research, 2024, 12(3): 205-222.
https://doi.org/10.46690/ager.2024.06.05

Abstract:
CO_2/N_2-enhanced coalbed methane recovery is an important means of increasing coalbed methane production, and understanding the competitive adsorption of CO_2, CH_4 and N_2 in coalbeds and its impact on coal properties is important. A structural model for anthracite from Daning-Jixian was constructed based on elemental analyses, Fourier-transform infrared spectroscopy, X-ray photoelectron spectroscopy and carbon nuclear magnetic resonance data. The grand canonical Monte Carlo method was used to research the competitive adsorption of multiple gases on coal and changes in the porosity and permeability. These results indicated that with increasing CO_2 injection, considerable methane desorption occurred in the coal seams, and the porosity and permeability of the coal decreased. During N_2 injection, the adsorption of methane on the coal increased, and the porosity and permeability of the coal increased gradually. However, the desorption rate of CH_4 after injection of N_2 was much lower than that after injection of CO_2. With CO_2 and N_2 injection, as the molar mass ratio of N_2 to CO_2 increased, the quantity of CO_2 adsorbed decreased, and the total amount of gas adsorbed on the coal decreased, which increased the porosity of the coal. At an the molar mass ratio of N_2 to CO_2 is 0.6, the desorption rate of CH_4 was 70.95%, the porosity and permeability of the coal were high, and considerable CO_2 was sequestered to mitigate greenhouse gas emissions and provide economic and environmental benefits.

1. Introduction

Coalbed methane (CBM) is both a hazard to coal mining safety and a source of clean, high-quality energy, but it is also a greenhouse gas. According to statistics, the amount of CBM buried at depths of 1,000-3,000 m is 2.87 times that buried at depths less than 1,000 m (Li et al., 2023a). Therefore, CBM at depths of 1,000 m or greater is a guaranteed resource for the development of China's CBM industry (Xu et al., 2023), and it is highly important for ensuring coal mine safety, improving energy utilization efficiency, and protecting the atmosphere. Injecting carbon dioxide into geological formations can improve the recovery rate of shale gas and CBM and minimize global greenhouse gas emissions (Omotilewa et al., 2021). This is a feasible approach that combines the efficient exploitation of CBM with carbon capture and storage (Yasemi et al., 2023). CO_2-enhanced coalbed methane (CO_2-ECBM) technology has been widely applied in CBM extraction with significant benefits. However, CO_2 sequestration in coal causes coal matrix expansion (Hosking et al., 2020; Wang et al., 2023a), which reduces coalbed permeability (Talapatra, 2020; Jeong et al., 2023). This process makes subsequent gas injection more difficult and affects CBM production, which is even more detrimental to the development of low-permeability CBM reservoirs in China (Packham et al., 2012). Therefore, based on CO_2-ECBM technology, CO_2/N_2 gas injection was proposed to improve the CBM desorption rate by injecting a N_2/CO_2 mixture into a coalbed (Asif et al., 2022).

Yandy Scientific Press

*Corresponding author.
E-mail address: jn_pan@hpu.edu.cn (J. Pan); 17852642393@163.com (F. Jiao); feigongfu@yeah.net (K. Wang); liyunbo@hpu.edu.cn (Y. Li); dangyusong@hpu.edu.cn (D. Song); quhou@ucas.ac.cn (Q. Hou).

Received March 20, 2024; revised April 17, 2024; accepted May 9, 2024; available online May 15, 2024.

This technique increased the reservoir pressure, reduced the methane partial pressure, and improved methane production (Talapatra et al., 2021). The objective of N_2-enhanced coalbed methane is to enhance the pore volumes and permeabilities of coal reservoirs. CO_2-ECBM desorbs the CBM and injects captured CO_2 into deep, inaccessible coal reservoirs to reduce greenhouse gas purity (Liao et al., 2023), making it a useful countermeasure for mitigating emissions.

Understanding the process and effects of ECBM injection in coal seams depends on recognition of the interaction mechanisms between coal and gases. Therefore, it is essential to establish a rational coal molecular structure and explore the interaction mechanisms among coal and methane, carbon dioxide, and nitrogen (Ursueguía et al., 2021). Numerous researchers have interpreted the coal molecular structure model (CMSM) and characterized the carbon framework and functional groups through industrial analyses, elemental analyses, carbon nuclear magnetic resonance (^{13}C NMR) (Tursunov et al., 2020) spectroscopy, X-ray photoelectron spectroscopy (XPS) and attenuated total reflectance Fourier-transform infrared spectroscopy (FTIR) (Salmachi et al., 2023). Based on this, they reconstructed a coal molecular structure model (CMSM) and validated its correctness (Jia et al., 2023).

Based on the aforementioned approach, a comprehensive study was conducted to construct a CMSM and study the competitive adsorption of $CO_2/CH_4/N_2$ in coal seams with the grand canonical Monte Carlo (GCMC) method. Studies have demonstrated that coal has different affinities for different gases, which decrease in the order of $CO_2 > CH_4 > N_2$ (Sander et al., 2020). Through numerous displacement/competitive adsorption experiments and numerical simulations, it is believed that the equilibrium adsorption state of coal is independent of the injection sequence (Zhang et al., 2018; Wu et al., 2019). By applying the GCMC method and molecular dynamics (MD) method, the micromechanism by which CO_2 displaced CH_4 was investigated. During the CO_2 injection process, the increased isothermal heat due to CO_2 adsorption on coal made the overall adsorption system unstable, leading to a reduced capacity for CH_4 adsorption on the framework (Kang et al., 2022). Furthermore, with increasing CO_2 content within the mixed gas, the total amount adsorbed correspondingly increased, while the adsorption selectivity coefficient decreased. By establishing a finite element coupled dual-pore and dual-permeability model that integrated the flow and adsorption behaviour of multicomponent gases, it was found that the injection of pure CO_2 and N_2 could increase the desorption rate of shale gas by approximately 80% and 20%, respectively (Li and Elsworth, 2019; Dwivedi et al., 2023). Through adsorption-strain experiments, it was determined that the relationships between gas adsorption-induced swelling and total swelling are $\varepsilon_{CO_2} > \varepsilon_{CH_4} > \varepsilon_{N_2}$ (George and Barakat, 2001; Shen et al., 2023). Some scholars have investigated the competitive adsorption of CO_2 and CH_4 in medium-rank coal (Chakravarty et al., 2020; Wei et al., 2021; Mabuza et al., 2022). They discovered that, as the CO_2 pressure increased, the CH_4 concentration decreased initially and then stabilized. These findings suggested that the decreased CH_4 concentration was attributable to two main factors. First, in coal, the CO_2 adsorption capacity of coal is due to the adsorption capacity of CH_4, which increases the CH_4 recovery efficiency (Iddphonce and Wang, 2021). Second, the elevated CO_2 concentration functioned as a diluent, thereby diluting the remaining CH_4 (Long et al., 2021). An experiment was conducted to investigate the differential swelling ratio of the coal matrix resulting from multicomponent gas adsorption using molecular simulation and pore mechanics models. It was found that in the CO_2 and CH_4 binary system, the coal matrix swelling rate increased as the CO_2 mole fraction increased (Talapatra, 2020). Conversely, in the N_2/CH_4 binary system, the swelling rate decreased as the N_2 mole fraction increased (Neyertz and Brown, 2020).

Currently, in situ CBM enhancement through gas injection involves the direct injection of pure CO_2 into a coal seam. The source of pure CO_2 is difficult to guarantee, and the injection of pure CO_2 significantly reduces the permeability of the coal seam and weakens the mechanical properties of the coal (Thomas and Chen, 2024), which hinders subsequent continuous gas injection. Research on CO_2/N_2 mixtures has focused on the adsorption of multicomponent components on coal, but there is little research on the displacement of CBM by a CO_2/N_2 mixture, particularly quantitative analyses of the optimal injection ratio of CO_2/N_2.

Most of the abovementioned research involved molecular adsorption simulations with classical CMSM. The development of an independent CMSM specifically designed for simulations is relatively uncommon in the literature. Therefore, this research focused on the deep anthracite extracted from Well No. 8 of Daning-Jixian. Elemental analyses and XPS, ^{13}C NMR and FTIR spectroscopy were employed to analyse and study the coal samples and construct a molecular model. Using the methods of MD and GCMC, $CO_2/CH_4/N_2$ adsorption on CMSM and its impact on the physical properties of CMSM were simulated, and the transformation law was explored to determine the adsorption capacity, selectivity, porosity and permeability of CO_2/N_2-ECBM and the optimal CO_2/N_2 ratio. This article provides guidance for increasing the production of CBM in the field in Daning-Jixian.

2. Samples and experiments

2.1 Coal sample collection

The coal sample was collected from the No. 8 coal seam at Daning-Jixian in the Ordos Basin, and the vitrinite was handpicked and separated. Prior to experimentation, the sample was crushed, ground and sieved through a 200-mesh sieve. An elemental analyser was used to determine the elemental compositions of the coal samples, which included C, H, O, N and S. Table 1 shows the basic information of the coal samples, among them, M, A, V and FC are based on air-dry basis.

2.2 X-ray photoelectron spectroscopy

XPS was performed with a Thermo Scientific ESCALAB Xi+ X-ray photoelectron spectroscopy instrument. XPS spectra of the N and S in the coal were obtained. The vertical axis represents the number of electrons, and the horizontal axis re-

Table 1. Basic information of the coal samples.

Type	M	A	V	F_C	TOC	Pyrite	Other	C	H	O	N	S	$R_{O,\max}$
Content (%)	0.86	24.74	8.06	66.34	94.5	0.2	5.4	86.11	3.06	7.71	0.13	2.99	2.82

Notes: M, moisture; A, ash; V, volatile matter; F_C, fixed carbon; TOC, total organic carbon.

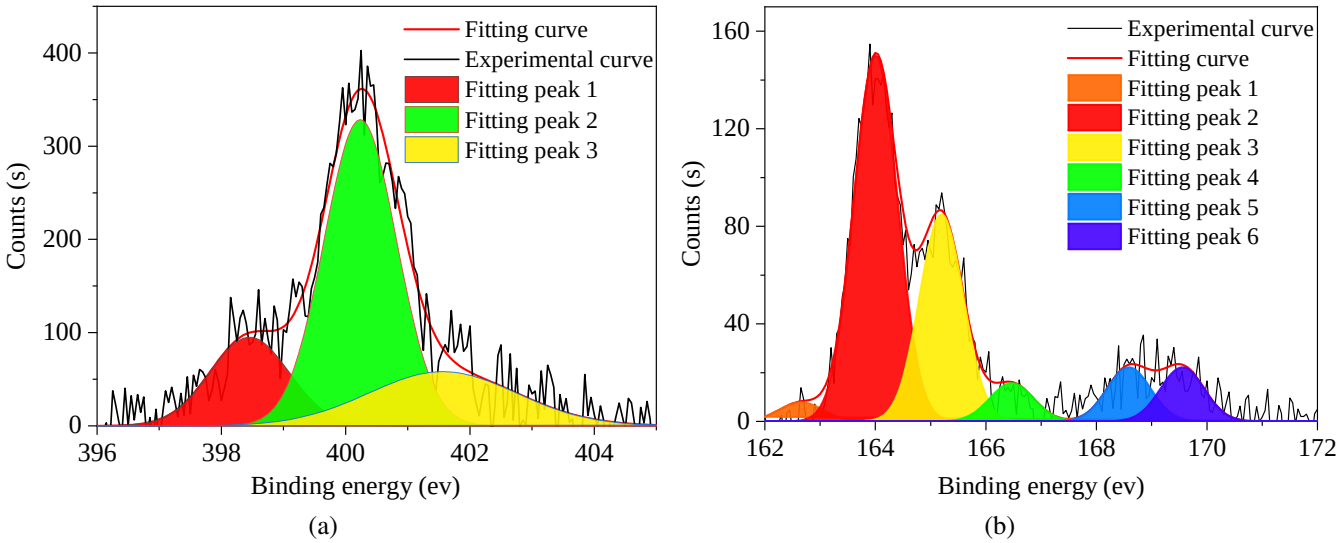

Fig. 1. (a) N (1s) peak deconvolution and (b) S (2p) peak deconvolution.

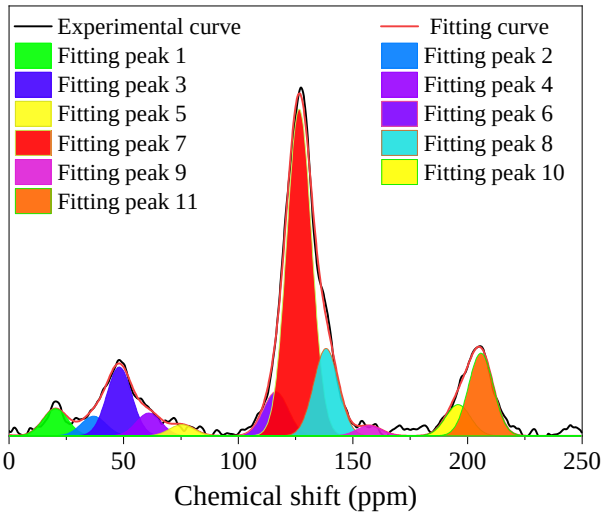

Fig. 2. ^{13}C NMR spectrum.

Table 2. ^{13}C NMR peak fitting parameters.

Chemical shift (ppm)	Attribution	Percentage (%)
20.25	Aliphatic methyl carbon	2.82
35.20, 45.32	Methylene carbon	4.31
56.29, 84.57	Oxygenated aliphatic carbon	6.48
113.12, 119.40, 128.70	Protonated aromatic carbon	39.18
137.51, 145.34	Alkylated aromatic carbon	29.24
154.86, 164.41	Alkylated aromatic carbon	7.80
198.39	Carboxyl	3.05
210.38	Carbonyl	7.12

presents the binding energy. By analysing the XPS spectra of N (1 s) (Fig. 1(a)) and S (2p) (Fig. 1(b)) in coal (Lu et al., 2023), the forms of different elements present were obtained.

The fitting results show that the nitrogen present in anthracite in Daning-Jixian is pyrrole-type, which is the main form of nitrogen, accounting for 83.32% of the total nitrogen content. The next highest proportion of nitrogen was associated with pyridine, at 12.34%. The lowest proportion was associated with seasonal nitrogen, at only 4.34%. Sulfur is present mainly in the form of thiophene sulfur (77.59%), supplemented by sulfoxide sulfur and inorganic sulfur, accounting for 7.33% and 7.32%, respectively, of the total sulfur content.

2.3 FTIR

FTIR spectra were obtained with a Thermo Scientific Nicolet S5 FTIR spectrometer produced in the United States. The potassium bromide pellet method was used to scan the range of 4,000 to 400 cm^{-1}. The spectrum was obtained by performing 128 scans with a cumulative resolution of 4 cm^{-1}.

Table 3. Structural characteristics of the coal sample.

Type	f_a	f_a^c	f_a'	f_a^N	f_a^H	f_a^P	f_a^S	f_a^B	f_{al}	f_{al}^*	f_{al}^H	f_{al}^O
Content (%)	87.57	7.36	80.21	54.49	25.72	7.02	21.58	25.89	12.43	2.82	4.31	5.31

Notes: f_a, total sp^2 hybridized C; f_a^c, carbonyl group or carboxyl group C; f_a', aromatic C; f_a^N, nonprotonated and aromatic C; f_a^H, protonated and aromatic C; f_a^P, aromatic C bonded to hydroxyl or ether oxygen; f_a^S, alkylated aromatic C; f_a^B, aromatic bridgehead C; f_{al}, total sp^3 hybridized C; f_{al}^*, $-CH_3$ or quaternary C; f_{al}^H, $-CH$ or $-CH_2$; f_{al}^O, aliphatic C bonded to oxygen.

The obtained infrared spectrum is shown in Fig. 3(a).

The infrared spectrum can be divided into four segments, which include peaks for aromatic structures (700-900 cm^{-1}), oxygen-containing functional groups (1,000-1,800 cm^{-1}), aliphatic structures (2,800-3,000 cm^{-1}), and hydroxyl groups (3,000-3,600 cm^{-1}) (Ghosh and Bandopadhyay, 2020; Boral et al., 2021; Kamble et al., 2022). After baseline correction, the selected regions of the spectra were subjected to peak fitting with Origin software (Li et al., 2023b) (Figs. 3(b)-3(e)).

Based on the aforementioned analysis, the molecular structure of anthracite predominantly consists of a tetra-substituted benzene ring and a five-substituted benzene ring (with a relative area ratio of 61.95%), followed by a tri-substituted benzene ring (with a relative area ratio of 33.03%). The aliphatic chain is primarily composed of methyl and methylene groups. The oxygen-containing functional group exhibits a phenol alcohol ether (C-O) to carboxyl group and carbonyl group (C=O) ratio of 9.6:1.

The aromatic carbon ratio refers to the proportion of carbon atoms in the coal that are present in aliphatic and aromatic components (Phan et al., 2021). It can be calculated with Eqs. (1), (2), and (3) and the peak areas of the infrared spectrum (Ibarra et al., 1996):

$$f_a' = 1 - \frac{C_{al}}{C} \tag{1}$$

$$\frac{C_{al}}{C} = \frac{\frac{H_{al}}{H}\cdot\frac{H}{C}}{\frac{H_{al}}{C_{al}}} \tag{2}$$

$$\frac{H_{al}}{H} = \frac{A_{3,000-2,800}}{(A_{3,000-2,800}+A_{700-900})} \tag{3}$$

where C_{al}/C represents the relative content of aliphatic carbon as a proportion of the total carbon; H/C denotes the ratio between hydrogen and carbon atoms, determined with elemental analyses; H_{al}/H denotes the ratio between the aliphatic hydrogen content and total hydrogen content; and H_{al}/C_{al} denotes the ratio between hydrogen and carbon atoms in fatty clusters, with an empirical value of 1.8.

2.4 ^{13}C NMR

^{13}C NMR experiments were performed with a Bruker 600 M superconducting nuclear magnetic resonance spectrometer. The ^{13}C NMR spectra within the chemical shift range of -10 to 250 ppm were subjected to peak fitting with Origin software (Jaiswal et al., 2021; Yang et al., 2021), as illustrated in Fig. 2.

Table 4. Aromatic carbonan functional group types.

Aromatic carbon structure	Number	Oxygenated functional groups	Number
Thiophene	3	O−H	5
Anthracene	1	C−O	4
Pyrene	4	C=O	5
Benzopyrene	4	COOR	1

The assignments of chemical shifts for various carbon structures and the relative percentages in the ^{13}C NMR spectrum of the coal are shown in Table 2 (Wang et al., 2021).

Accordingly, the 12 structural characteristics of the coal were computed (Lu et al., 2023) and are summarized in Table 3. The ratio of bridging carbons to peripheral carbons (X_{BP}) in CMSMs is an indicator of the extent of condensation and ring fusion within the aromatic ring structure of the coal. This ratio can be utilized to estimate the sizes of aromatic clusters present in coal (Ping et al., 2020). The calculation formula is provided below:

$$X_{BP} = \frac{f_a^B}{f_a^H + f_a^P + f_a^S} \tag{4}$$

The relevant parameters from Table 3 substituted into Eq. (4) yielded a value of 0.476 for the parameter X_{BP}. This value can be used to characterize the sizes of the aromatic clusters in the sample.

3. Molecular model construction

3.1 Establishment of a 2D molecular model of coal

In the aforementioned analysis, X_{BP} was determined to be 0.476. Therefore, in the coal molecular model proposed in this study, the main aromatic structures consisted of pyrene, biphenyl, and a small amount of anthracene, with the addition of a small quantity of thiophene. By considering different combinations of aromatic structural units and calculating the corresponding value of X_{BP} for each combination, the types and quantities of aromatic structural units that yielded the closest match to the experimental data for X_{BP} were determined. These findings are summarized in Table 4.

According to Table 4, 186 aromatic carbon atoms were present in the DJ CMSMs. Considering that f_a' was 80.21%,

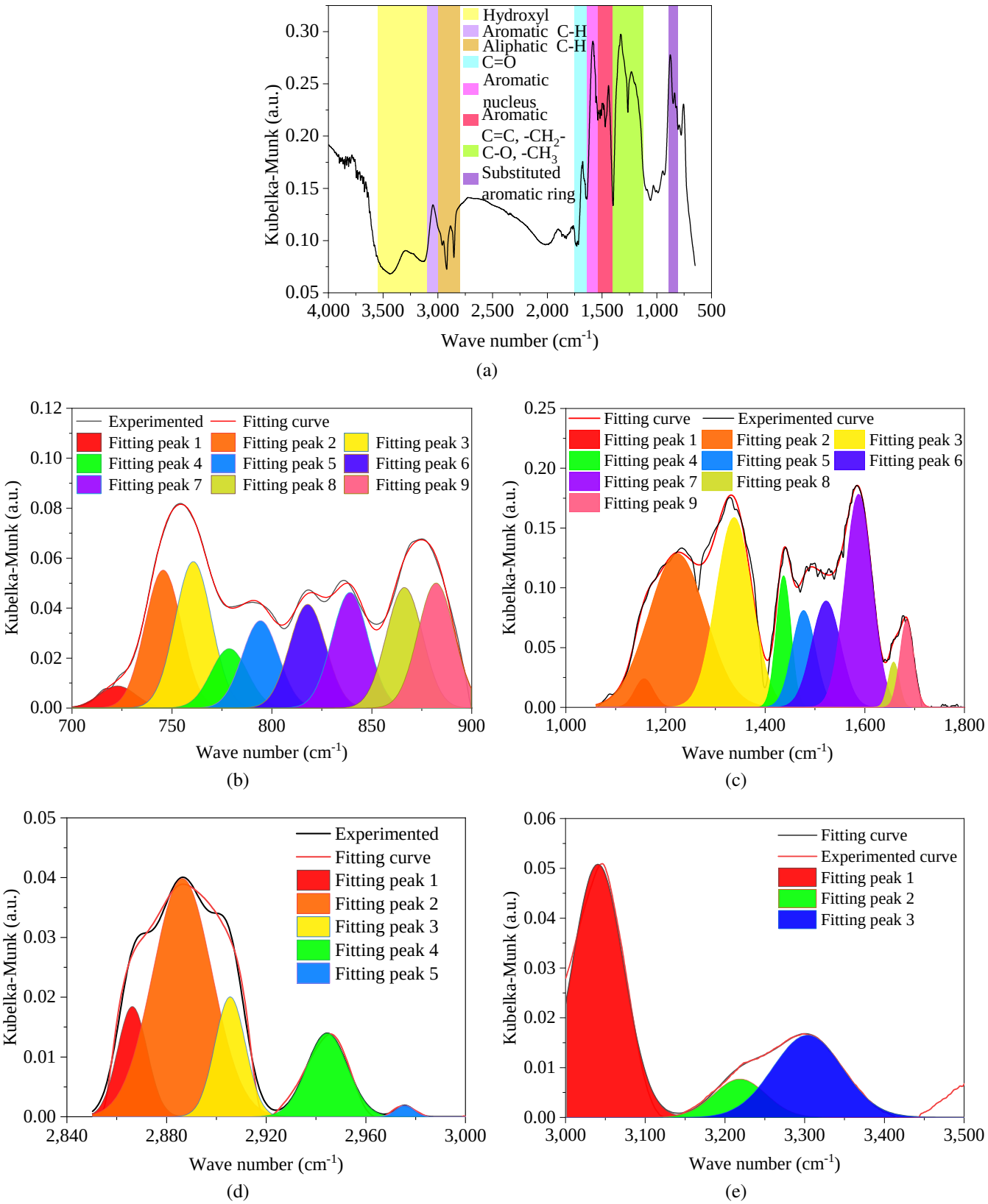

Fig. 3. (a) Total infrared spectrum, (b) 700-900 cm^{-1} infrared spectrum, (c) 1,000-1,800 cm^{-1} infrared spectrum, (d) 2,840-3,000 cm^{-1} infrared spectrum and (e) 3,000-3,500 cm^{-1} infrared spectrum.

the total number of carbons in the CMSM was 231. Consequently, the number of aliphatic carbons, carboxyl group carbons, and carbonyl group carbons in the CMSM was 45. The aliphatic structures in the coal comprised aliphatic side chains, cycloalkanes, and hydrogenated aromatic rings. It is evident from the table that the values of f_{al}^{H} and f_{al}^{*} for the sample were 4.31% and 2.82%, respectively, indicating that the ratio of methyl to methylene groups in the structural model was approximately 1.5.

According to the ratios of the various elements in the DJ element assay and the number of carbon atoms determined with the previous coal molecular model, the numbers of oxygen, nitrogen, and sulfur atoms were determined to be 15, 0, and 2, respectively. XPS revealed that the coal sample primarily contained pyrrolic nitrogen and thiophenic sulfur as the predominant forms of nitrogen and sulfur, respectively. Combined with the results from ^{13}C NMR, the ratios of oxygen substitution, oxygen-containing aliphatic carbon, carboxyl carbon, and carbonyl carbon were approximately 6.5 : 7.8 : 3.0 : 7.1, which indicated the presence of 4 hydroxyl groups, 5 oxygen-containing aliphatic groups, 1 carboxyl group, and 5 carbonyl groups in the bituminous coal.

Based on the results for each element, a coal molecule model was built with Materials Studios software. The ^{13}C NMR spectra of the coal molecules were calculated with MestReNova software to adjust the sites and concatenation methods of various functional groups by comparing the calculated ^{13}C NMR spectra with the experimental spectra. The aim was to achieve consistency between the established coal molecule model and the experimental ^{13}C NMR spectrum (Fig. 4(a)). According to Table 3, f_a' was 80.21%, with a bridge carbon ratio of 0.476. The corresponding values for the model in Fig. 4(b) were 79.39% and 0.476, respectively. Therefore, the molecular formula of the DJ anthracite was $C_{231}H_{158}O_{16}S_3$, with a molecular weight of 3273.96, and the structure of the coal molecule is shown in Fig. 4(b).

3.2 Establishment of the 3D coal molecular model

The COMPASS II molecular force field was selected for MS simulations, with customized calculation precision and force field-assigned charges. NVT ensemble dynamics (300-600 K, 10 cycles) were employed. The obtained coal molecular model was subjected to multiple geometric optimizations, annealing treatments, and MD simulations using the Forcite module to obtain the global energy minimum and most stable coal molecular spatial model. The time is 2,000 ps, and the step length is 1 fs. The energy of the system is monitored during the simulation to ensure that the simulation time is long enough and that the simulation converges. Using the Amorphous Cell module, four coal molecular models were randomly placed into the unit cell with an initial density of 0.1 g/cm^3 (Feng et al., 2021). The MD method combined with the annealing algorithm was used to optimize the simulation. The time step was 0.5 fs, and the total simulation time was 500 ps. The energy and density of the system were detected during the simulation to ensure convergence. The time–density diagram is shown in Fig. 4(c), and the cell density of coal is calculated to be 1.54 g/cm^3 by taking the equilibrium region in the second half of the diagram. The equilibrium configuration of CMSM was determined, and the cell parameters were $23 \times 23 \times 23$ Å^3 (Zhang et al., 2020).

3.3 Verification of the coal molecular model

The adsorption capacity calculated in MS is the absolute adsorption capacity, while the adsorption capacity obtained in the experiment is the excess adsorption capacity. Therefore, according to Eq. (5), the absolute adsorption capacity and the excess adsorption capacity are converted:

$$N_{ex} = N_{ad} - V \cdot \rho \tag{5}$$

where N_{ex} is the excess adsorption amount, g; N_{ad} is the absolute adsorption amount, g; ρ is the adsorbent density at a certain temperature and pressure, g/cm^3; V is the pore volume of the adsorbent, cm^3, calculated from the atomic volume and surface; and He (diameter = 0.26 nm) with poor adsorption is selected as the probe. The GCMC method was used to simulate the isothermal adsorption curve of CH_4 within the CMSMs at a temperature of 333.15 K. Based on these results, the fitted data were compared with the experimentally measured data. Fig. 5 shows the isothermal adsorption data obtained from the molecular simulation and the Langmuir fitting equation. The fitting results were compared with the experimentally determined Langmuir volume and Langmuir pressure, as shown in Fig. 5. In conclusion, mutual verification of the carbon NMR spectra, density, Langmuir volume, and Langmuir pressure demonstrated that the coal molecular model represented the coal in an actual block.

3.4 Simulation scheme and parameter setting

The coal seam is located at a depth of 1,800 m underground, with a surface temperature of 298 K and a surface pressure of 0.1 MPa. Therefore, the average temperature of the coal seam is 343 K (with a geothermal gradient of 2.5 K/100 m), and the reservoir pressure is 16.2 MPa (with an underground pressure gradient of 0.98 MPa/100 m (Isaka and Ranjith, 2020)). Based on the CH_4 isothermal adsorption curve, the saturation adsorption capacity was calculated to be 1.24 mmol/g. To investigate the effects of CO_2 or N_2 injection on methane adsorption and coal reservoir properties, the molar weight of CH_4 was kept constant at 1.24 mmol/g in the mixed gas, and the CO_2 or N_2 injection pressure was adjusted to vary the molar mass ratio of CO_2 or N_2 to CH_4 (expressed by $\omega_{CO_2}/\omega_{CH_4}$,or $\omega_{N_2}/\omega_{CH_4}$) within the range of 0 to 1.5, with a sampling interval of 0.1, resulting in a total of 15 groups. The fugacity values of each component were calculated at various temperatures and pressures with the GERG-2008 gas state equation in Aspen Plus software (Figs. 6(a) and 6(b)).

To simulate the influence of injecting the CO_2 and N_2 mixture on the adsorption, pore volume and permeability characteristics of the coal, the molar methane concentration in the gas mixture was kept constant at 1.24 mmol/g. The coal molecular model was based on a 1 : 1 molar ratio of CO_2 to methane. At an CO_2 and N_2 mixed gas is injected, the N_2

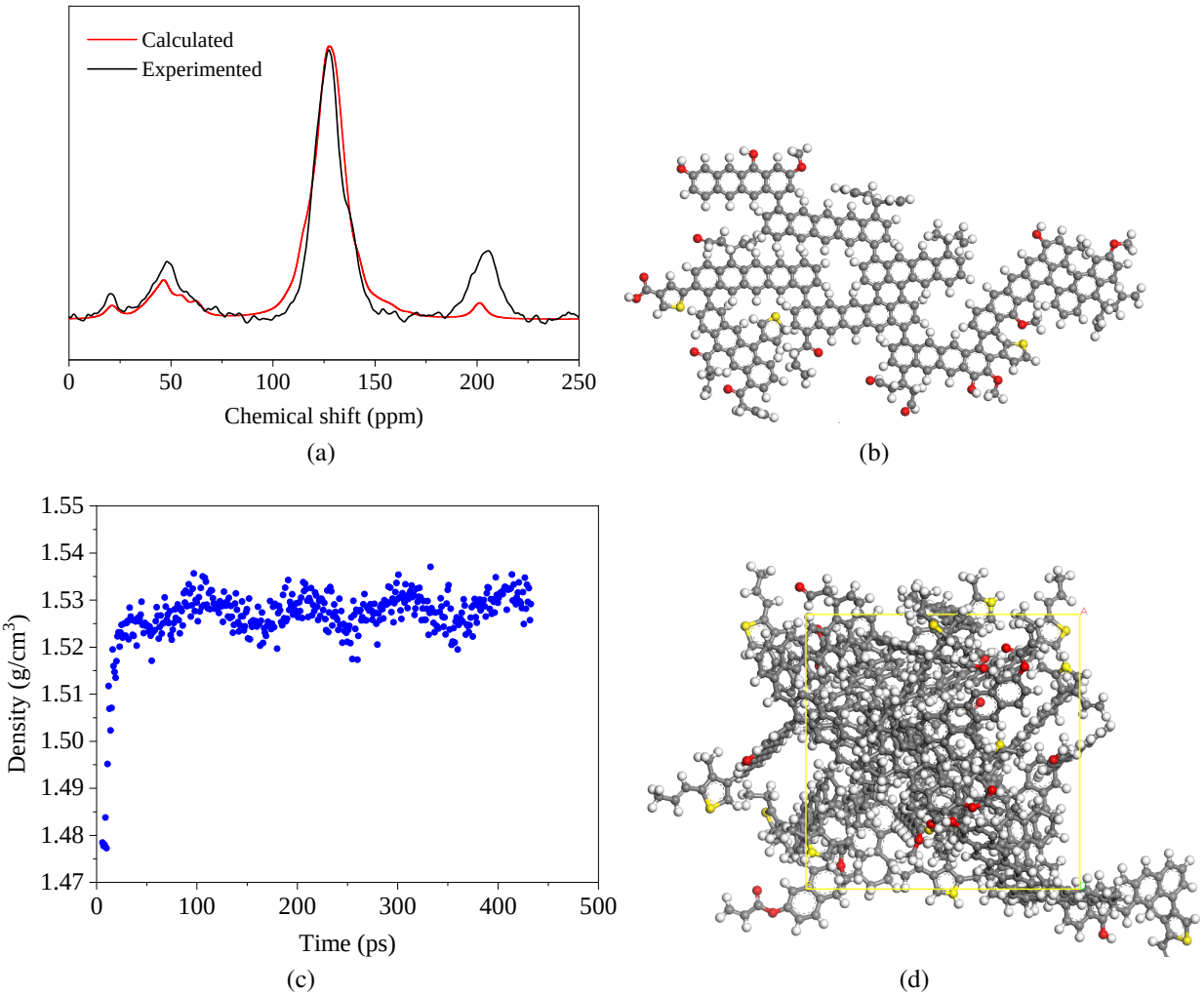

Fig. 4. (a) Experimental and modelled ^{13}C NMR spectra, (b) Plane model of the molecular structure of coal from Daning-Jixian, (c) density-time diagram and (d) coal polymer cell model (red, yellow, black and white represent oxygen, sulfur, carbon and hydrogen, respectively).

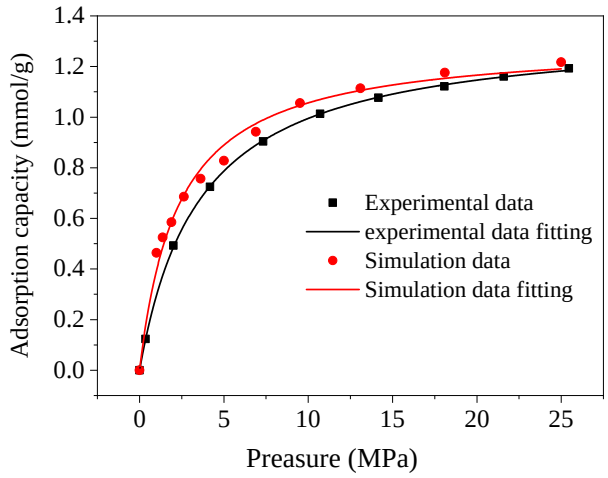

Fig. 5. Isothermal adsorption curve for the model.

pressure is adjusted to change the molar mass ratio of N_2 to CO_2 (expressed by $\omega_{N_2}/\omega_{CO_2}$) in the range of 0 1, resulting in a total of 10 groups. The fugacity of each component was calculated with Aspen Plus software with the GERG-2008 gas state equation (Fig. 6(c)).

The sorption module was used to calculate the adsorption of CH_4 by the CO_2/N_2 binary gas mixture, as well as its impact on the pore volume and permeability within the coal. The sorption module was configured with the following specific parameter settings: the task type was fixed pressure, the method was Metropolis, and the simulation accuracy was customized. For the adsorption calculation, 1×10^7 conformations were generated initially for equilibration, followed by the generation of another 1×10^7 conformations for averaging the actual adsorption quantity, resulting in a total of 2×10^7 conformations. The COMPASS II force field was selected as the molecular force field, and the charge calculation method was set to Forcefield assigned. The summation methods for the electrostatic and van der Waals forces were Ewald- and atom-based, respectively. The fugacities of CH_4, CO_2 and N_2 were set according to Fig. 6.

To investigate the impact of CO_2/N_2 on the porosity of the CMSM, the Connolly algorithm was first employed with He

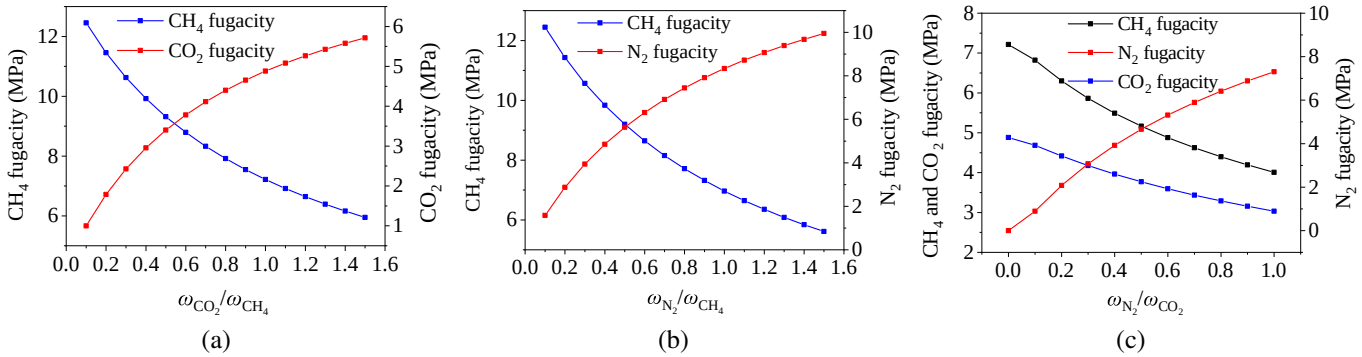

Fig. 6. (a) Fugacity of each component with $\omega_{CO_2}/\omega_{CH_4}$, (b) the fugacity of each component changes with the $\omega_{N_2}/\omega_{CH_4}$ curve and (c) the fugacity of each component with the $\omega_{N_2}/\omega_{CO_2}$ change curve.

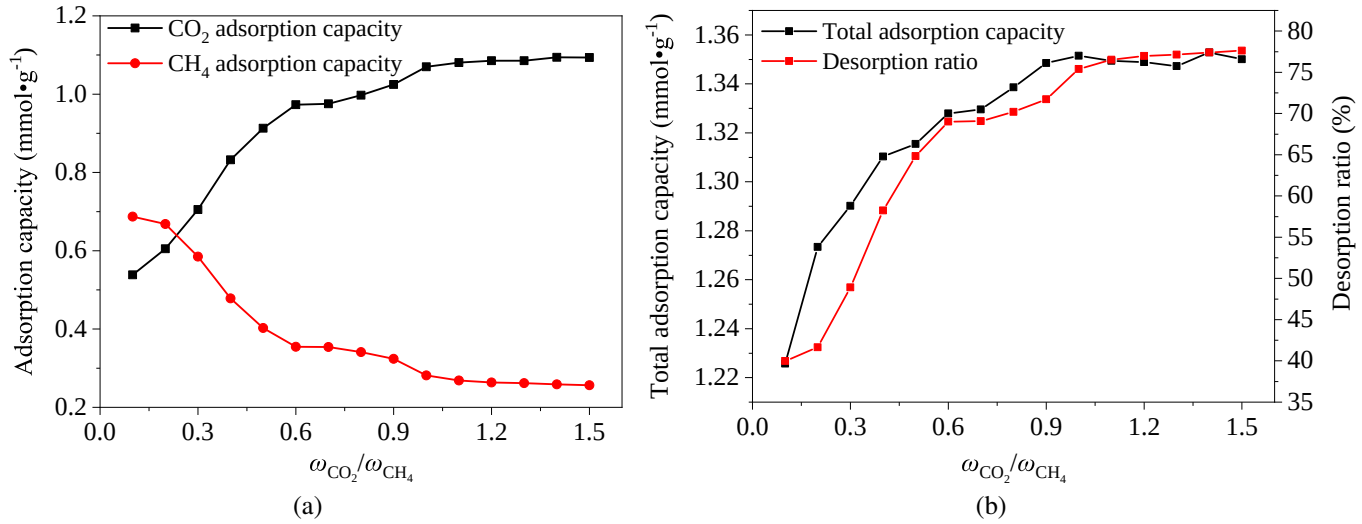

Fig. 7. (a) Plots of the CO_2 and CH_4 adsorption capacities and (b) total adsorption capacity and CH_4 desorption rate.

molecules as molecular probes to determine the pore volume of the CMSM. Some scholars (Chilingar et al., 1963; Liu et al., 2011) have proposed that the matrix permeability of coal is proportional to the cube of the porosity when the porosity is less than 10%:

$$\frac{k}{k_0} = \left(\frac{\varphi}{\varphi_0}\right)^3 \tag{6}$$

where k is the matrix permeability of the coal, and the unit is 10^{-3} μm^2; φ is the matrix porosity of the coal, and the unit is %; k_0 is the initial permeability of the coal matrix, and the unit is 10^{-3} μm^2; and φ_0 is the initial porosity of the coal matrix, and the unit is %.

The gas adsorption selectivity coefficient measures the affinity of coal for a specific gas component within a mixed gas (Karimi et al., 2021; Serafin et al., 2022). The formula used to calculate the adsorption selectivity coefficient ($S_{i/j}$) is (Rainone et al., 2021):

$$S_{i/j} = \frac{\frac{x_i}{x_j}}{\frac{y_i}{y_j}} \tag{7}$$

where x_i and x_j represent the molar quantities of components i and j in the adsorbed phase of the system, respectively, while y_i and y_j represent the molar quantities of components i and j in the gas phase of the system, respectively. The adsorption phase value is expressed by the adsorption amount. Since Langmuir monolayer molecular adsorption follows, the bulk phase is calculated by multiplying the gas density by the free space volume.

4. Results and discussion

4.1 Effects of CO_2 injection on CH_4 adsorption, coal porosity and permeability

4.1.1 CH_4 adsorption

Fig. 7(a) shows the correlation between the CH_4 and CO_2 adsorption capacities with respect to $\omega_{CO_2}/\omega_{CH_4}$ for the CMSM. Additionally, Fig. 7(b) depicts the total gas adsorption capacity and CH_4 desorption rate of the coal molecular model. The difference in adsorption capacity between CH_4 in the mixed system and pure CH_4 represents the quantity of CH_4 desorbed. Overall, as $\omega_{CO_2}/\omega_{CH_4}$ increased, the adsorption

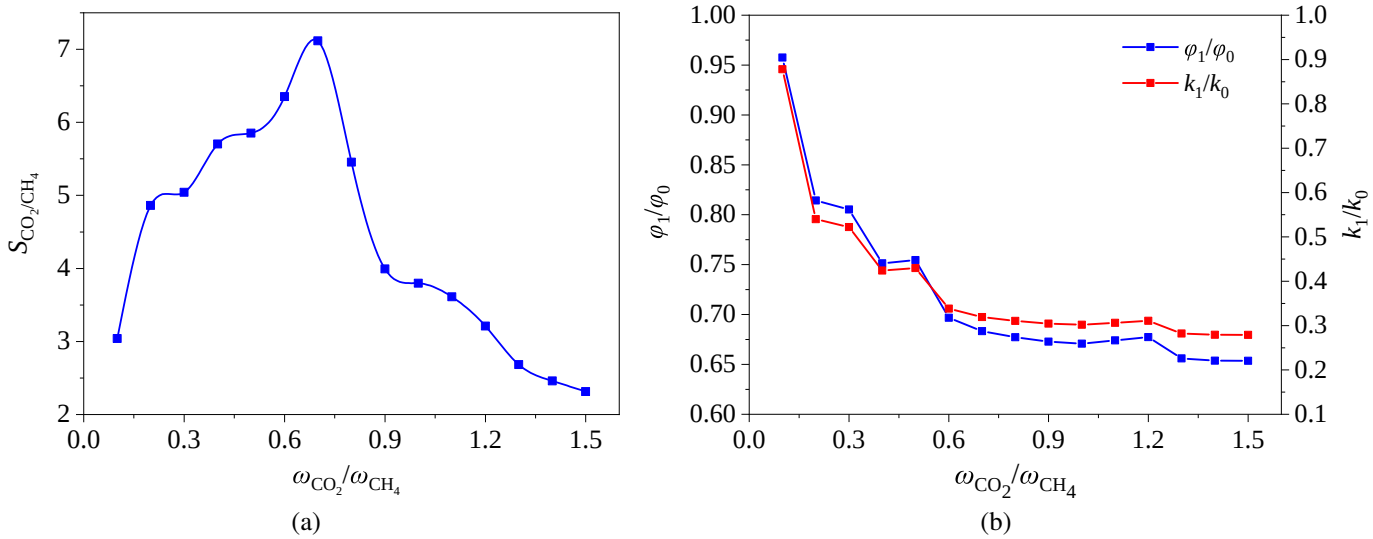

Fig. 8. (a) Adsorption selection coefficient for the CO_2 and CH_4 mixed system and (b) porosity and permeability of the coal after CO_2 injection.

capacity of CH_4 decreased, while the adsorption capacity of CO_2 increased. When $\omega_{CO_2}/\omega_{CH_4}$ was in the range of 0 to 0.6, the CH_4 adsorption capacity rapidly decreased to 0.355 mmol/g, while the CO_2 adsorption capacity significantly increased to 0.973 mmol/g, with a CH_4 desorption rate of 69.02%. After $\omega_{CO_2}/\omega_{CH_4}$ reached 0.6, the decreasing trends for the CH_4 and CO_2 adsorption capacities slowed and gradually stabilized. When $\omega_{CO_2}/\omega_{CH_4} = 1.5$, the adsorption capacity of CO_2 was 1.094, and that of CH_4 was 0.256 mmol/g, with a CH_4 desorption rate of 77.61%. When $\omega_{CO_2}/\omega_{CH_4}$ was less than 0.3, the adsorbed content of CH_4 was greater than that of CO_2. When a mixed gas competes for adsorption on the coal surface, the adsorption capacities of the individual gas components depend on their own adsorption characteristics and on the partial pressures of the individual gas components. The injection of CO_2 led to a stable increase in the total amount of gas adsorbed by the CMSM (Fig. 7(b)). When $\omega_{CO_2}/\omega_{CH_4} < 0.9$, the overall ability of the coal to adsorb gases increased as CO_2 injection increased. However, once the $\omega_{CO_2}/\omega_{CH_4}$ ratio reached 0.9, the rate of increase in the total adsorption capacity slowed significantly.

The coal molecular model exhibited strong physical heterogeneity. The coal matrix pore surface was composed of a mixture of adsorption sites, which had high energy and low energy and influenced the adsorption of the gas components and the overall amount of gas adsorbed (Gao et al., 2023). Because CO_2 has a greater adsorption capacity on the coal pore surface than does CH_4 (Sander et al., 2020), the coal substrate surface was more likely to adsorb CO_2, which weakened the interactions between the coal matrix and CH_4. During competitive adsorption, CO_2 molecules take up high-energy adsorption sites, displacing methane with the remaining adsorption sites and subsequently leading to desorption. From the perspective of methane adsorption at different gas ratios, the first stage corresponded to desorption from sites with high adsorption energies, while the second stage corresponded to desorption from sites with low adsorption energies. Therefore, during the initial injection of CO_2, CO_2 occupied the adsorption sites with high energy, displacing CH_4, and the gas pressure effect caused a decrease in the CH_4 partial pressure, leading to the rapid desorption of CH_4 and an increase in the adsorbed CO_2 content. During the later stages of CO_2 injection, the number of adsorption sites decreased, and the partial pressure, which was due to methane, continuously decreased as the $\omega_{CO_2}/\omega_{CH_4}$ ratio increased. As a result, the decreasing trend for the CH_4 adsorption capacity gradually levelled, and the ability of the coal to adsorb CO_2 reached saturation. Therefore, during the later stages of CO_2 injection, the adsorbed contents of CO_2 and CH_4 exhibited gradual changes.

Fig. 8(a) shows the S_{CO_2/CH_4} values for the sorption of the different CO_2/CH_4 binary gas mixtures on the coal samples. The results indicated that the adsorption selectivity coefficient S_{CO_2/CH_4} ranged from 2.31 to 7.11, and all were greater than 1, indicating that the coal samples had a stronger adsorption affinity for CO_2 than for CH_4 under competitive adsorption conditions (Liu and Wilcox, 2012). This confirmed the feasibility of implementing CO_2-ECBM technology in coal seams. The S_{CO_2/CH_4} value first increased and then decreased as the molar amount of CO_2 injected increased. This behaviour was attributed to the combined influence of energy effects (adsorption energy) and entropy effects (filling effect) (Salmachi et al., 2023). In the ascending phase, the dominant factor was the energy effect, as the interaction of CO_2 with coal was more powerful than that of CH_4 with coal. The coal substrate surface more easily adsorbs CO_2, which causes an upwards trend in the selectivity coefficient curve for gas adsorption. However, as the $\omega_{CO_2}/\omega_{CH_4}$ ratio increased, the high-energy adsorption sites were more rapidly engaged by CO_2, and the remaining adsorption sites had weaker adsorption capacities for gas molecules. The entropy effect became the dominant factor affecting adsorption. Additionally, the simulation results indicated that when $\omega_{CO_2}/\omega_{CH_4}$ exceeded 0.7,

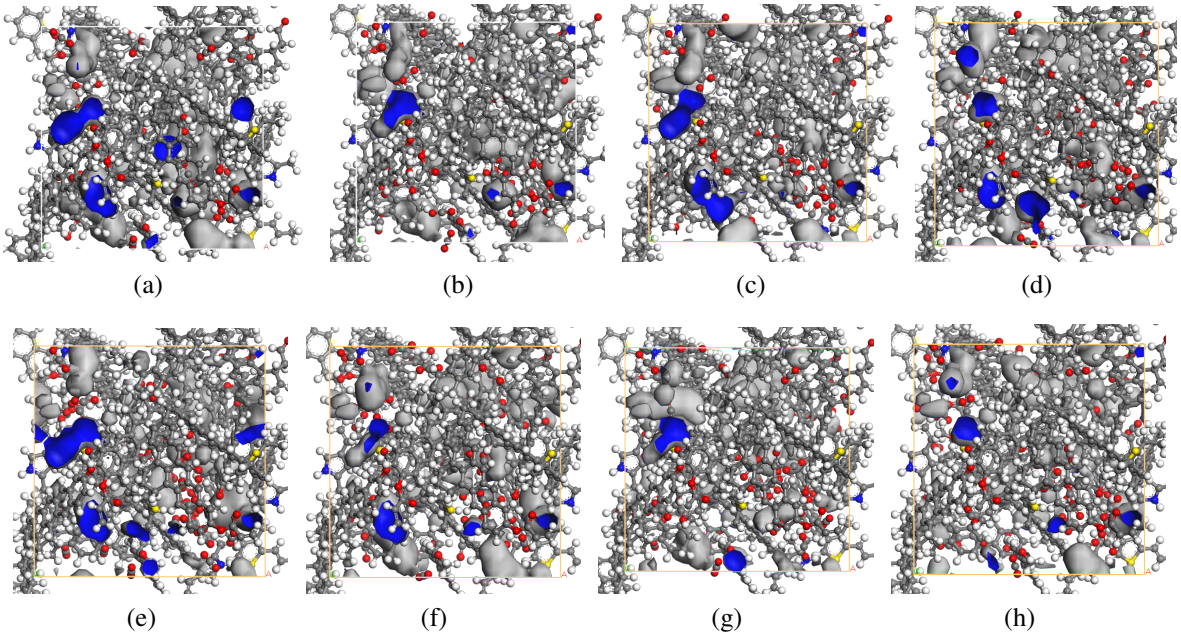

Fig. 9. Pore structure of coal under different $\omega_{CO_2}/\omega_{CH_4}$ conditions: (a) 0 (φ = 8.07%),(b) 0.2 (φ = 6.57%), (c) 0.4 (φ = 6.06%), (d) 0.6 (φ = 5.62%), (e) 0.8 (φ = 5.47%), (f) 1.0 (φ = 5.41%), (g) 1.3 (φ = 5.29%) and (h) 1.5 (φ = 5.27%)(the blue area shows the pores, and the grey area shows the pore surface).

S_{CO_2/CH_4} decreased when the CO_2 coefficient increased in the gas mixture. This suggested that a high CO_2 concentration had an inhibitory effect on S_{CO_2/CH_4}.

The injection of high-pressure CO_2 increased the plasticity of the coal matrix while inducing a rearrangement of the CMSM, resulting in irreversible damage to the CMSM (Pan et al., 2019). In this experimental setup, when $\omega_{CO_2}/\omega_{CH_4} \geq 0.8$, CO_2 reached the supercritical state ($ScCO_2$). The low viscosity, high diffusion coefficient, and zero surface tension of supercritical CO_2 facilitated large-scale carbon dioxide sequestration and a high desorption rate for CBM. However, as a result of the continuous injection of carbon dioxide, the coal matrix underwent continuous swelling that reduced the permeability of the coal (Hamza et al., 2021), which in turn affected subsequent CO_2 injection and hindered the diffusion of CH_4; this hindered the extraction of CH_4 and the storage of CO_2 (Su et al., 2021). From an engineering safety perspective, although increasing the CO_2 injection pressure could increase CO_2 storage, the CO_2 would gradually become saturated after exceeding the critical pressure, and CO_2 storage augmentation would be limited. Moreover, due to the substantial decrease in the physical properties of coal, the possibility of inducing coal seam fractures due to ground stress increases, potentially leading to CO_2 diversion (Wang et al., 2020). Based on multiple considerations, the use of an injection pressure near the critical point pressure may be the most favourable approach for ensuring both CO_2 storage and reducing the need for carbon dioxide diversion.

4.1.2 Porosity and permeability of the coal

The coal cell pore volumes were determined for different $\omega_{CO_2}/\omega_{CH_4}$ ratios with the MS software Connolly algorithm (Fig. 9) to analyse the change in the pore volume of the coal after gas adsorption. When CO_2 was not injected, the CMSMs were saturated with adsorbed CH_4, with a porosity φ of 8.07%, as shown in Fig. 9(a).

When $\omega_{CO_2}/\omega_{CH_4}$ = 0.6, the porosity of the coal decreased significantly to 5.62% (Fig. 9(d)). When $\omega_{CO_2}/\omega_{CH_4} \geq 0.7$, the pore distribution of the coal was stable, the porosity slowly decreased, and the final porosity was 5.27% (Fig. 9(h)).

Based on the cubic law and in combination with the Connolly algorithm, the dependence of the molecular porosity of coal on $\omega_{CO_2}/\omega_{CH_4}$ was calculated, and the changes in the coal matrix permeability were obtained. As shown in Fig. 9(b), when $\omega_{CO_2}/\omega_{CH_4}$ was in the range of 0 to 0.6, it had a significant impact on the coal porosity and permeability, with the maximum reduction.

When $\omega_{CO_2}/\omega_{CH_4}$ = 0.6, the coal molecular porosity decreased significantly to 5.62% (Fig. 9(d)). The porosity and permeability decreased by 30.32% and 66.17%, respectively. When $\omega_{CO_2}/\omega_{CH_4} \geq 0.7$, the distribution of coal pores stabilized, and the porosity slowly decreased, eventually reaching 5.27% (Fig. 9(h)). Additionally, the porosity and permeability decreased by 34.64% and 72.08%, respectively. The decreasing trends for the coal properties were consistent with the trend for the total amount of adsorbed gas. Previous studies involving experiments and actual production (Oudinot et al., 2011) have shown that injecting a large amount of CO_2 into coal usually leads to a 60% to 90% decrease in coal seam permeability (Salmachi et al., 2023). Compared to the actual decrease in permeability, the simulated results were slightly lower. This is because the study considered only the influence of coal expansion on the coal properties and did not account for variations in the effective stress, and the

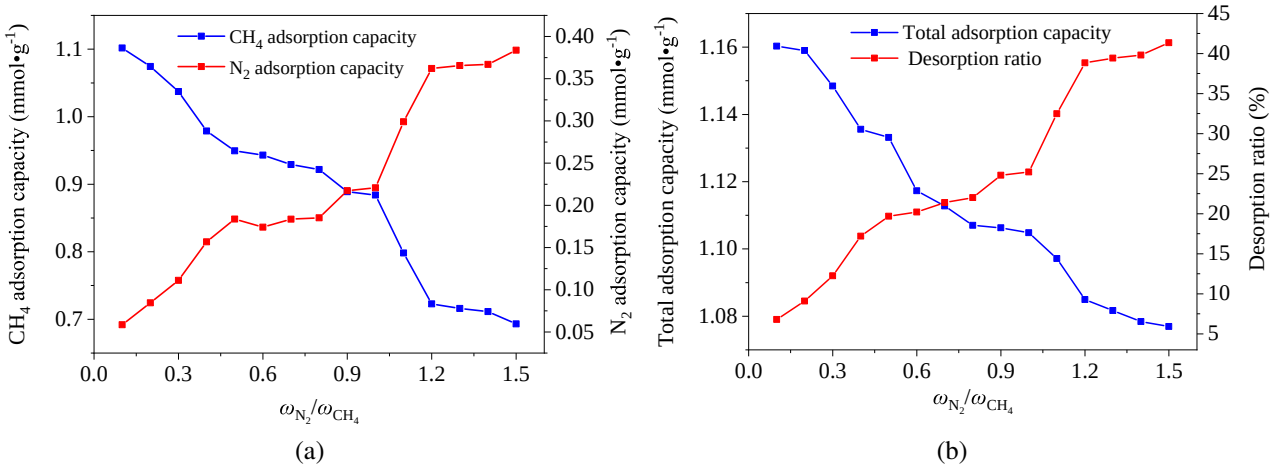

Fig. 10. (a) N_2 and CH_4 adsorption capacities and (b) total amount adsorbed and the CH_4 desorption rate.

amount of CO_2 was much smaller than the actual volume injected during production. Therefore, these simulation results accurately represent the damage caused by CO_2 to coal seam permeability in practical terms.

In summary, in the deep coal reservoir at a depth of 1,800 m, the optimal injection pressure for CO_2 displacement of CH_4 was 0.6 to 0.8 times that of CH_4. This range ensured a high CH_4 desorption rate of 69.02% to 71.65% while minimizing damage to the coal reservoir.

4.2 Effect of N_2 injection on CH_4 adsorption, coal porosity and permeability

4.2.1 CH_4 adsorption

Plots of CH_4 and N_2 adsorption in the CMSM versus $\omega_{N_2}/\omega_{CH_4}$ are shown in Fig. 10(a), and the total gas adsorption and CH_4 desorption rate in the CMSM are presented in Fig. 10(b). Overall, the adsorption of CH_4 and N_2 showed a linear relationship with increasing $\omega_{N_2}/\omega_{CH_4}$. As $\omega_{N_2}/\omega_{CH_4}$ increased, CH_4 adsorption decreased, while N_2 adsorption increased. Specifically, CH_4 adsorption decreased from an initial value of 1.182 mmol/g to 0.693 mmol/g, while N_2 adsorption increased to 0.384 mmol/g. The maximum CH_4 desorption rate was 41.36%. N_2 adsorption never exceeded CH_4 adsorption, indicating that N_2 has a weaker adsorption affinity than CH_4 when competing for adsorption sites on the coal surface.

In the coal matrix, the total amount of adsorbed gas decreased as the molar amount of N_2 injected increased. The trend for total adsorption was dominated by CH_4 adsorption, indicating that the coal matrix had a greater adsorption capacity for CH_4 than for N_2. As shown in Fig. 10(a), the quantity of CH_4 desorbed increased with increasing N_2 injection, indicating that N_2 injection induced desorption and diffusion of CH_4. N_2 injection created pressure differences in different regions, providing kinetic energy for free CH_4 transport through pore fissures (Hajianzadeh et al., 2023; Wang et al., 2023b). This disrupted the dynamic equilibrium for CH_4 on the coal matrix surface and intensified the conversion of CH_4 from the adsorbed to the free state, leading to the migration of free CH_4 and decreasing the amount of CH_4 adsorbed. Furthermore, the increasing partial pressure of N_2 significantly increased the probability of collisions between N_2 molecules and the CMSM surface due to thermal motion. N_2 gas molecules in the free state can be adsorbed on the coal surface via van der Waals forces. Macroscopically, N_2 injection can displace and replace CH_4. This indicated that during the ECBM process, gas molecules with weaker adsorption affinities could displace gas molecules with stronger adsorption affinities from the coal surface when the pressure was high enough. Moreover, the results also demonstrated the feasibility of increasing the CH_4 desorption rate with N_2 injection at the molecular level.

Through comparative calculations, it was found that the maximum desorption rate after injecting CO_2 reached 77.61%, which was significantly greater than the maximum desorption rate of 41.36% seen after injecting N_2. This indicated that the injection of CO_2 into a coal reservoir could more efficiently increase the ratio of CH_4 desorption than the injection of N_2. When the same proportion of N_2 was injected, the amount of CH_4 desorbed from the CMSM was not as significant as that observed when CO_2 was injected. Only when the pressure of N_2 was 1.5 times that of coalbed gas did the ratio of CH_4 desorption exceed 40%. This suggested that, to increase the extraction of CH_4 from coal via N_2 injection, the gas partial pressure must reach a certain minimum value to achieve the desired effect. The reason for the different effects on CH_4 extraction from the two gases was that the mechanisms for N_2 and CO_2 displacing CH_4 in the coal reservoirs were completely different. When CO_2 is injected into a coal reservoir, its adsorption affinity on the coal surface is greater than that of CH_4, so even a small amount of CO_2 can displace the adsorbed CH_4 (Skoczylas et al., 2020). When N_2 is injected into a coal reservoir, although its adsorption capacity is weaker than that of CH_4, it is also controlled by the partial pressure of CH_4 desorbed from the coal reservoir. High-pressure N_2 injection reduces the effective partial pressure of CH_4, thereby inducing desorption (Hajianzadeh et al., 2023). Additionally, high-pressure N_2 competes with

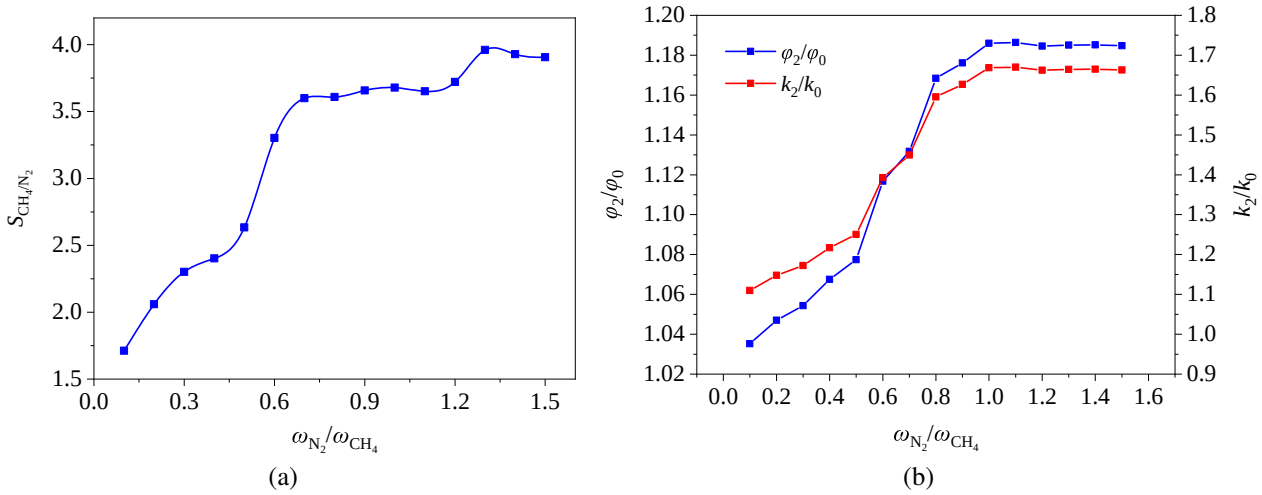

Fig. 11. (a) Adsorption selection coefficient in the N_2 and CH_4 mixed system and (b) coal pores and permeability after injection of N_2.

CH_4 for adsorption. Therefore, when N_2 is used to enhance CH_4 extraction, the partial pressure of N_2 must reach a certain level to achieve the desired effect. However, during on-site N_2 injection, excessively high pressures increase the risk of CH_4 outbursts (Li et al., 2021). Therefore, measures such as predrainage and pre-extraction should be implemented to reduce CH_4 pressure and ensure safe production.

Fig. 11(a) shows that the S_{CH_4/N_2} ratio ranged from 1.71 to 3.96, which was greater than 1, indicating that under competitive adsorption conditions, CH_4 was more strongly adsorbed than N_2. Although both CH_4 and N_2 are nonpolar gases, CH_4 has a slightly greater polarizability than N_2, resulting in stronger interactions between CH_4 and the coal reservoir (Qadir et al., 2022). As a result, the CH_4 adsorption capacity decreases, and the number of unsaturated sites with high adsorption energies increases. The kinetic diameter of CH_4 is greater than that of N_2, and CH_4 experiences greater steric hindrance from the coal matrix pores than does N_2. These factors collectively influence S_{CH_4/N_2}, which increases as $\omega_{N_2}/\omega_{CH_4}$ increases. This indicates that a higher molar fraction of N_2 increases the SCH_4/N_2 ratio. Combining the above information, it was concluded that an increase in the proportion of strongly adsorbing components in a gas mixture reduces the adsorption competitiveness of the weakly adsorbing component during competitive adsorption.

4.2.2 Porosity and permeability

The pore volumes of a coal crystal cell at different N_2 molar fractions were determined with the Connolly algorithm in MS software (Fig. 12). When no N_2 was injected, the CMSM were saturated with adsorbed CH_4, resulting in a porosity of $\varphi_0 = 8.068\%$ and a pore distribution as shown in Fig. 9(a). As the $\omega_{N_2}/\omega_{CH_4}$ ratio increased, the porosity of the CMSM linearly increased to 9.576% (Fig. 12(g)), representing an increase of 18.47% compared to the initial porosity.

Based on the cubic law and in combination with the Connolly algorithm, the molecular porosity of coal as a function of $\omega_{N_2}/\omega_{CH_4}$ can be calculated, and the changes in the coal matrix permeability can be obtained. As shown in Fig. 12(b), when $\omega_{N_2}/\omega_{CH_4}$ was in the range of 0 to 0.8, the coal pore size and permeability increased significantly, with the porosity and permeability increasing by 16.84% and 59.51%, respectively. However, after $\omega_{N_2}/\omega_{CH_4}$ exceeded 0.8, the effect of N_2 injection on the porosity and permeability of the coal decreased. Ultimately, compared to those of the saturated CH_4 coal sample, the porosity and permeability increased by 18.47% and 66.31%, respectively.

In the saturated CH_4 coal sample without N_2 injection, the adsorbed pores, flow channels, and fracture surfaces in the coal caused coal matrix expansion and deformation. A reduced fracture aperture and even closure resulted in a lower initial permeability. N_2 first induced the desorption of CH_4 from low-energy adsorption sites through a partial pressure effect, causing the coal matrix to undergo desorption-induced shrinkage. During this stage, the amount of CH_4 desorbed was relatively low, leading to a gradual increase in the permeability. When $0 < \omega_{N_2}/\omega_{CH_4} < 0.8$, the coal permeability increased rapidly. Due to the differences in the N_2 partial pressure and CH_4 concentration, the adsorbed CH_4 in the coal reservoirs desorbed rapidly, causing the further contraction of the coal reservoir and increasing pore fracture. During this stage, the desorption rate of CH_4 increased, resulting in an increased rate of coal volume shrinkage and permeability recovery.

4.3 Effects of CO_2 and N_2 mixed gas injection on CH_4 adsorption, coal porosity and permeability

During the process of actual gas injection to enhance CBM desorption, it was difficult to guarantee a pure CO_2 gas source. Moreover, injecting pure CO_2 gas significantly reduced the coalbed permeability, blocked CH_4 diffusion and flow, and made subsequent gas injection difficult. As a result, the desorption rate could not reach an ideal state. On the other hand, injected pure N_2 could prematurely break through the coal reservoir, resulting in a greater proportion of N_2

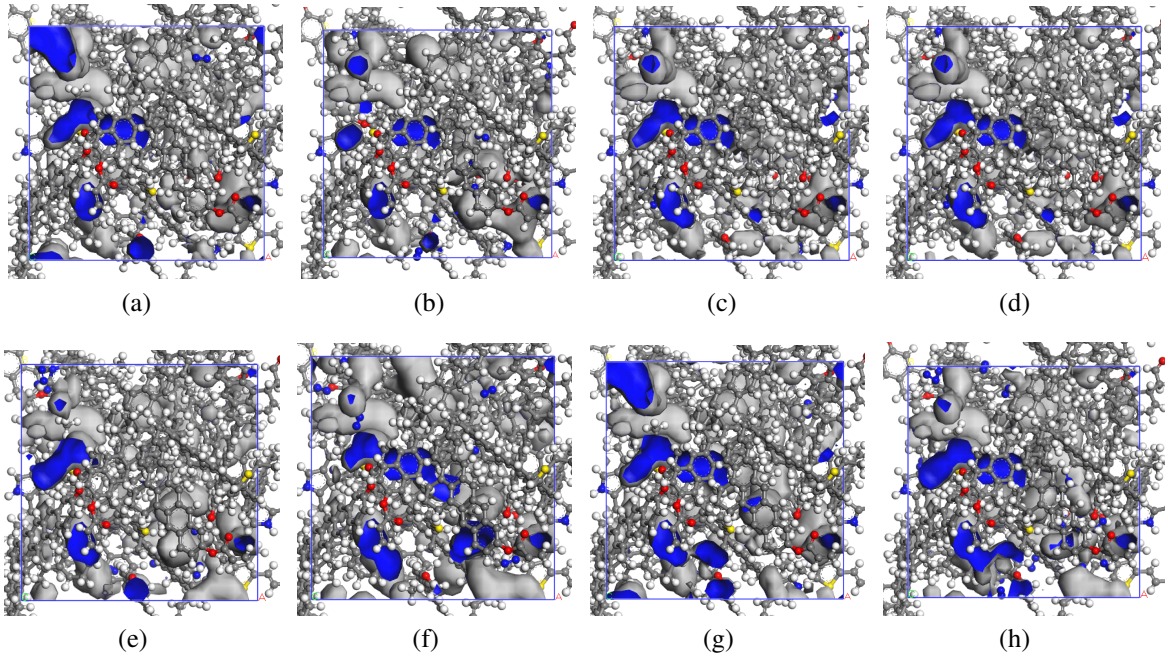

Fig. 12. Pore structure of coal under different $\omega_{N_2}/\omega_{CH_4}$ conditions: (a) 0.1 (φ = 8.35%), (b) 0.3 (φ = 8.51%), (c) 0.5 (φ = 8.69%), (d) 0.7 (φ = 9.13%), (e) 0.9 (φ = 9.49%), (f) 1.1 (φ = 9.56%), (g) 1.3 (φ = 9.57%) and (h) 1.5 (φ = 9.58%).

in the produced CH_4 gas. This would increase the difficulty and cost of subsequent purification, which has unfavourable economic consequences. Therefore, injecting CO_2 and N_2 in different proportions is proposed for the permeation of CH_4 in coal reservoirs. By utilizing the strong competitive adsorption effect and permeability-enhancing effect of N_2, an appropriate gas injection ratio can be selected to maximize the CBM desorption rate.

4.4 CH_4 adsorption

The quantities of CH_4, CO_2 and N_2 adsorbed by the CMSM varied with the $\omega_{CO_2}/\omega_{N_2}$ ratio, as shown in Fig. 13(a). With increasing $\omega_{CO_2}/\omega_{N_2}$, the quantity of N_2 adsorbed linearly decreased, the quantity of CH_4 adsorbed initially decreased and then stabilized, and the quantity of CO_2 adsorbed first dramatically increased after those levels were removed. For a coal reservoir, the total amount of adsorbed gas is calculated by summing the amounts of each component adsorbed, as shown in Fig. 13(b). The total amount adsorbed increased from 1.184 to 1.262 mmol/g when $\omega_{CO_2}/\omega_{N_2} \leq 0.4$, with a CH_4 desorption amount of 0.64 mmol/g and a desorption rate of 55.92%. When $0.4 < \omega_{CO_2}/\omega_{N_2}$, the total amount adsorbed slowly increased to 1.29 mmol/g, followed by a slight decrease, and it eventually stabilized at 1.28 mmol/g. The maximum desorption rate during the adsorption–desorption process was 61.89% at $\omega_{CO_2}/\omega_{N_2}$ = 0.9. The transformation curve for the total amount of adsorbed gas was similar to the curve for the amount of CO_2 adsorbed as a function of the $\omega_{N_2}/\omega_{CO_2}$ ratio in Fig. 13(a), indicating that CO_2 played a dominant role in changing the total amount of CO_2 adsorbed.

The greatest reduction in CH_4 adsorption occurred when $0 < \omega_{CO_2}/\omega_{N_2} \leq 0.4$, with a CH_4 desorption rate of 55.92% occurring at $\omega_{CO_2}/\omega_{N_2} = 0.4$; the amount of CO_2 adsorbed had already surpassed that of CH_4. This was because CO_2, which had the strongest interactions with the coal matrix, rapidly occupied the high-energy adsorption sites, which released CH_4. Simultaneously, the increased diffusion of N_2 in the gas mixture enhanced the desorption and diffusion of CH_4.

When $0.4 < \omega_{CO_2}/\omega_{N_2} < 0.9$, the amount of CH_4 adsorbed continued to decrease, but the rate of decrease was much smaller than that when $\omega_{CO_2} \leq 0.4$. The amount of CH_4 adsorbed decreased from 0.55 mmol/g and stabilized at 0.53 mmol/g. At $\omega_{CO_2}/\omega_{N_2}$ = 0.9, the CH_4 desorption rate was 61.89%. During this stage, there were two factors influencing CH_4. First, although the pressure of CO_2 injection escalated, after the saturation of the high-energy adsorption sites in the coal matrix, CO_2, CH_4 and N_2 competed for adsorption at low-energy adsorption sites. Second, the molar ratio of N_2 gradually decreased in the gas mixture, resulting in a weakened diffusion effect. Additionally, the coal matrix expansion caused by the large amount of adsorbed CO_2 decreased the adsorption surface area and the number of adsorption sites. Furthermore, during the adsorption of gas molecules, the adsorbed state, free state, and desorbed state were in dynamic equilibrium. CO_2, which has a competitive adsorption advantage due to its significant heat of adsorption, actually hindered further CO_2 adsorption and released some of the competitive adsorption sites, thereby increasing the amount of CH_4 adsorbed. The aforementioned factors collectively determined the changes in CH_4 adsorption.

4.4.1 Porosity and permeability characteristics

The impact of CO_2/N_2 mixed injection on the coal porosity and permeability was investigated with the Connolly algo-

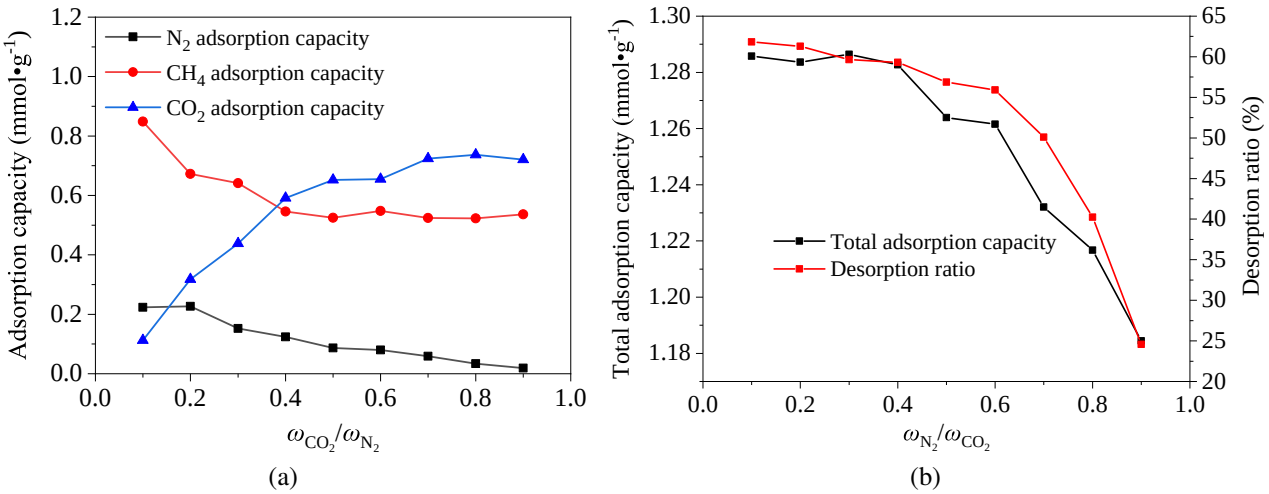

Fig. 13. (a) Plots of the adsorption capacities of CO_2, CH_4 and N_2 and (b) total adsorption capacity and CH_4 desorption rate.

rithm, as shown in Fig. 15. The coal porosity was positively correlated with the mole fraction of N_2 in the mixed gas. When no N_2 gas was added ($CO_2 : CH_4 = 1 : 1$), the porosity of the coal saturated with adsorbed CH_4 and CO_2 was $\varphi_1 = 6.089\%$, and the distribution of coal porosity is shown in Fig. 14.

Fig. 15 shows the variations in coal porosity and permeability caused by saturated adsorption of CH_4 on the coal, represented by the porosity φ_0 and permeability k_0 (Fig. 15(a)), as well as the ratio of the porosity φ_1 and permeability k1 of coal saturated with CH_4 and CO_2 without N_2 addition (Fig. 15(b)), at different $\omega_{N_2}/\omega_{CO_2}$ ratios. Fig. 15(b) shows that, overall, the injection of N_2 suppressed the coal matrix expansion caused by CO_2, thereby increasing the coal porosity and permeability.

When $\omega_{N_2}/\omega_{CO_2} \leq 0.3$, the injection of N_2 did not have apparent positive effects on the coal porosity and permeability. At this stage, the porosity was 6.82%, and the porosity and permeability recovered to 1.12 times and 1.41 times their values before N_2 injection, respectively. This was because although the proportion of CO_2 decreased and N_2 had the opposite effect, the increased permeability due to N_2 enlarged the coal matrix pores, exposing more abundant adsorption sites and leading to a slight increase in CO_2 adsorption. Based on the occupation of adsorption sites by CO_2, molecular heat effects, and N_2 partial pressure, the quantity of CH_4 adsorbed decreased, resulting in a stable overall gas adsorption capacity in the coal matrix. A small amount of N_2 suppressed the expansion of the coal matrix caused by CO_2 adsorption without effectively modifying the coal reservoir or increasing the porosity and permeability. As a result, swelling of the coal matrix due to adsorption was reduced, leading to an increase in the coal porosity due to coal matrix contraction.

When $0.3 < \omega_{N_2}/\omega_{CO_2} \leq 0.6$, the overall decrease in total adsorption was slightly slower than that observed when the $\omega_{N_2}/\omega_{CO_2}$ ratio was between 0.7 and 1. As a result, the expansion of the coal matrix due to gas adsorption decreased, and an increase in the proportion of the N_2 component enlarged the coal pores and increased the permeability. The porosity was 7.19%, and the pore size and permeability recovered to 1.18 times and 1.65 times their values before N_2 injection, respectively. At this stage, the desorption rate of CH_4 was 70.95%. When $0.6 < \omega_{N_2}/\omega_{CO_2} < 1$, the amount of CO_2 adsorbed decreased linearly, and eventually, the pore size and permeability recovered to 1.45 times and 3.04 times their values before N_2 injection, respectively. Especially when $0.8 \leq \omega_{N_2}/\omega_{CO_2} < 1$, the coal porosity and permeability recovered to the level of saturated methane adsorption in the coal reservoir after N_2 injection. This was mainly because N_2 injection led to desorption based on the N_2 partial pressure, resulting in a smaller total amount of gas adsorbed for the mixed gas system relative to gas adsorption when methane was saturated. This weakened the coal matrix expansion attributed to gas adsorption. However, at this stage, the desorption rate of CH_4 decreased linearly.

In summary, a N_2/CH_4 pressure ratio of 0.4 to 0.6 should be maintained during the mixed gas displacement process. The desorption rate of CH_4 should be between 59.64% and 55.92%. Additionally, a higher CO_2 sequestration capacity ensures the maintenance of favourable coal seam properties, which is beneficial for CBM development.

5. Conclusions

In this study, the molecular structure of Daning-Jixian coal was constructed. MD and GCMC were used to simulate the process of injecting different proportions of CO_2 and N_2 gas (single component and two component) into coal to promote CH_4 desorption, as well as changes in the porosity and permeability of the CMSM. The main conclusions are as follows:

1) During CO_2 displacement to enhance CBM production, increased CO_2 injection caused desorption of a significant amount of methane, and the desorption rate gradually increased to 77.61%. On the other hand, the total amount of gas adsorbed on the CMSM increased, leading to coal matrix expansion and decreases in coal porosity and permeability. When $\omega_{CO_2}/\omega_{CH_4} \geq 0.8$, the total amount

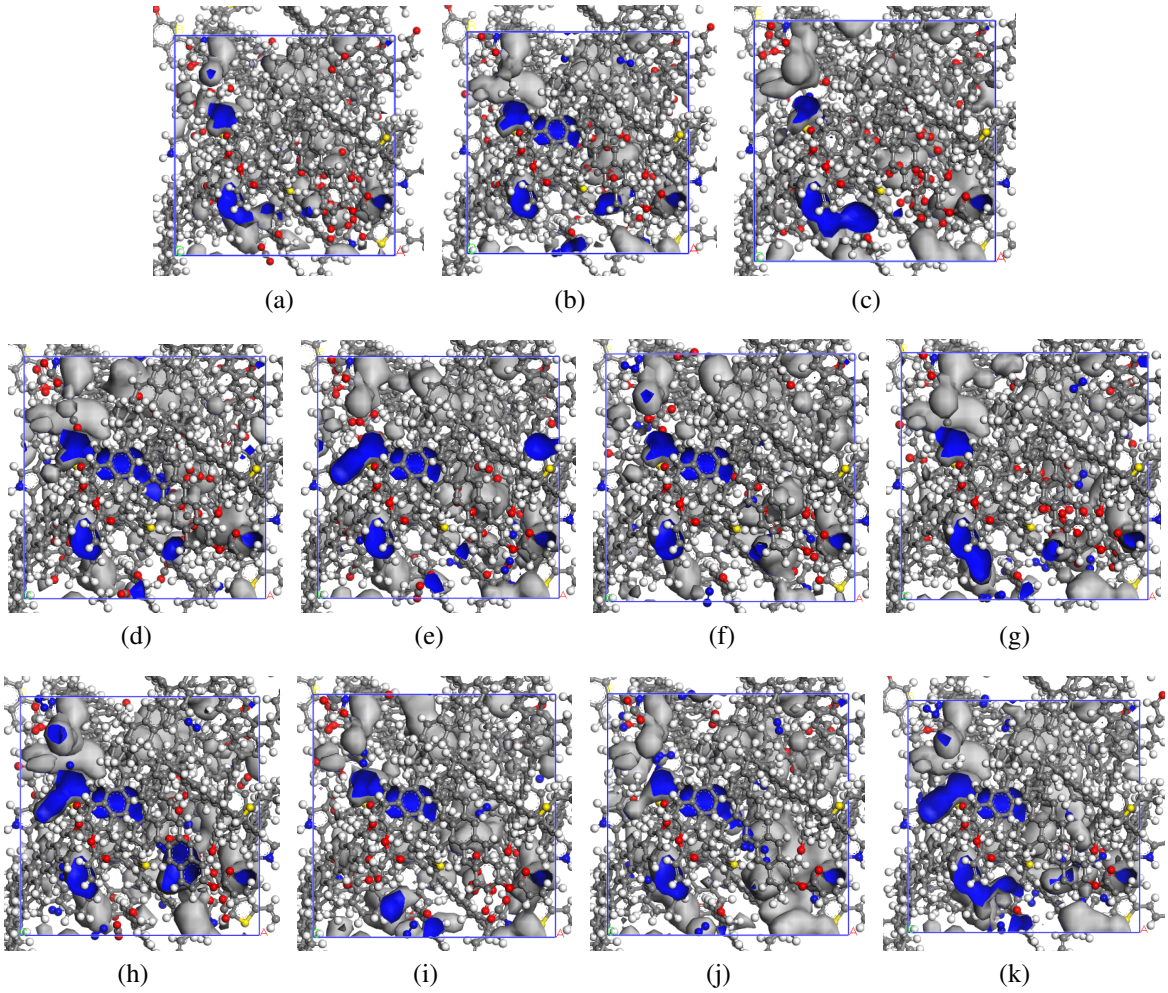

Fig. 14. Pore structure of coal under different $\omega_{N_2}/\omega_{CO_2}$ conditions: (a) 0 (φ = 6.09%), (b) 0.1 (φ = 6.80%), (c) 0.2 (φ = 6.81%), (d) 0.3 (φ = 6.82%), (e) 0.4 (φ = 6.93%), (f) 0.5 (φ = 6.99%), (g) 0.6 (φ = 7.19%), (h) 0.7 (φ = 7.20%), (i) 0.8 (φ = 8.15%), (j) 0.9 (φ = 8.82%) and (k) 1 (φ = 8.99%).

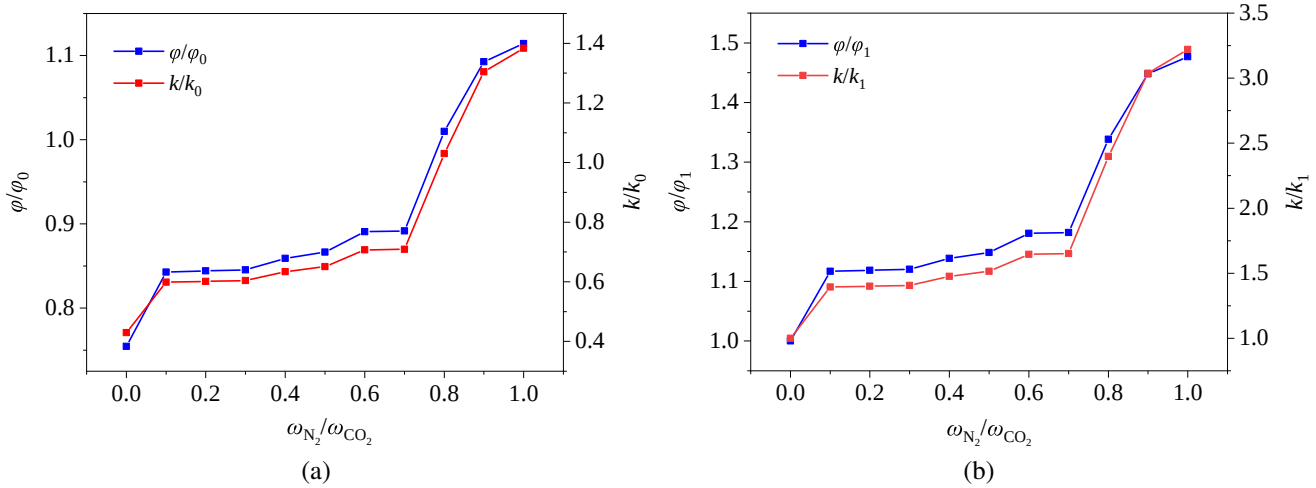

Fig. 15. (a) The ratio of coal pores and permeability after CO_2 and N_2 injection to that during pure CH_4 saturation and (b) the ratio of coal pores and permeability characteristics after CO_2 and N_2 injection to those during CO_2:CH_4 = 1:1 saturation.

of gas adsorbed on the coal and the coal porosity volume were relatively stable.

2) While injecting N_2 to enhance CBM production, a significant amount of methane was desorbed with increasing N_2 injection, and the methane desorption rate gradually increased and reached a maximum desorption rate of 41.36%. On the other hand, the total amount of gas adsorbed in the coal matrix decreased, leading to coal matrix contraction, and the porosity increased to 9.56%.
3) During the process of injecting the CO_2/N_2 mixture to enhance CBM production, the maximum desorption rate of methane was 73.49%. As the N_2 content increased, the methane desorption rate gradually decreased, and the pore volume and permeability of the coal increased. When $\omega_{N_2}/\omega_{CO_2} \geq 0.6$, the methane desorption rate decreased. When $\omega_{N_2}/\omega_{CO_2} \leq 0.6$, the porosity and permeability of the coal matrix remain low. Therefore, when $\omega_{N_2}/\omega_{CO_2}$ was 0.6, the CH_4 desorption rate was 70.95%, the coal porosity and permeability were greater, and the CO_2 sequestration capacity was significant, which decreased the greenhouse gas content.

Acknowledgements

This work was supported by the National Natural Science Foundation of China (No. 42072195), Major Science and Technology Projects of Xinjiang Uygur Autonomous Region (No. 2023A01004) and the Bidding project of Shanxi Science and Technology Plan (No. 20201101001).

Conflict of interest

The authors declare no competing interest.

References

Asif, M., Wang, L., Wang, R., et al. Mechanisms in CO_2-enhanced coalbed methane recovery process. Advances in Geo-Energy Research, 2022, 6(6): 531-534.

Boral, P., Varma, A. K., Maity, S. Nitration of Jharia basin coals, India: A study of structural modifications by XRD and FTIR techniques. International Journal of Coal Science & Technology, 2021, 8: 1034-1053.

Chakravarty, S., Chakravarty, K., Mishra, V., et al. Characterization of chemical structure with relative density of three different ranks of coal from India. Natural Resources Research, 2020, 29(5): 3121-3136.

Chilingar, G. V., Main, R., Sinnokrot, A. Relationship between porosity, permeability, and surface areas of sediments. Journal of Sedimentary Research, 1963, 33(3): 759-765.

Dwivedi, A., Dwivedi, A., Kumar, A. Qualitative surface characterization of Indian permian coal using XPS and FTIR. International Journal of Coal Preparation and Utilization, 2023, 43(7): 1152-1163.

Feng, W., Li, Z., Gao, H., et al. Understanding the molecular structure of HSW coal at atomic level: A comprehensive characterization from combined experimental and computational study. Green Energy Environ, 2021, 6(1): 150-159.

Gao, C., Liu, D., Vandeginste, V., et al. Thermodynamic energy change and occurrence mechanism of multiple fluids in coal reservoirs. Energy, 2023, 283: 129089.

George, J. S., Barakat, M. A. The change in effective stress associated with shrinkage from gas desorption in coal. International Journal of Coal Geology, 2001, 45(2-3): 105-113.

Ghosh, A. K., Bandopadhyay, A. K. Formation of thermogenic gases with coalification: FTIR and DFT examination of vitrinite rich coals. International Journal of Coal Geology, 2020, 219: 103379.

Hajianzadeh, M., Mahmoudi, J., Sadeghzadeh, S. Molecular dynamics simulations of methane adsorption and displacement from graphenylene shale reservoir nanochannels. Scientific Reports, 2023, 13(1): 15765.

Hamza, A., Hussein, I. A., Al-Marri, M. J., et al. CO_2 enhanced gas recovery and sequestration in depleted gas reservoirs: A review. Journal of Petroleum Science and Engineering, 2021, 196: 107685.

Hosking, L. J., Chen, M., Thomas, H. R. Numerical analysis of dual porosity coupled thermo-hydro-mechanical behaviour during CO_2 sequestration in coal. International Journal of Rock Mechanics and Mining Sciences, 2020, 135: 104473.

Ibarra, J., Munoz, E., Moliner, R. FTIR study of the evolution of coal structure during the coalification process. Organic Geochemistry, 1996, 24(6-7): 725-735.

Iddphonce, R., Wang, J. Investigation of CO_2 and CH_4 competitive adsorption during enhanced shale gas production. Journal of Petroleum Science and Engineering, 2021, 205: 108802.

Isaka, B., Ranjith, P. G. Investigation of temperature-and pressure-dependent flow characteristics of supercritical carbon dioxide- induced fractures in harcourt granite: Application to CO_2-based enhanced geothermal systems. International Journal of Heat and Mass Transfer, 2020, 158: 119931.

Jaiswal, Y., Pal, S. L., Jaiswal, H., et al. An investigation of changes in structural parameters and organic functional groups of inertinite rich lignite during acid treatment processes. Energy Sources, Part A: Recovery, Utilization, and Environmental Effects, 2021, in press, https://doi.org/10.1080/15567036.2021.1923867.

Jeong, S. R., Park, J. H., Lee, J. H., et al. Review of the adsorption equilibria of CO_2, CH_4, and their mixture on coals and shales at high pressures for enhanced CH_4 recovery and CO_2 sequestration. Fluid Phase Equilib, 2023, 564: 113591.

Jia, J., Wang, D., Li, B., et al. Molecular simulation study on the effect of coal metamorphism on the competitive adsorption of CO_2/CH_4 in binary system. Fuel, 2023, 335: 127046.

Kamble, A. D., Mendhe, V. A., Chavan, P. D., et al. Insights of mineral catalytic effects of high ash coal on carbon conversion in fluidized bed Co-gasification through FTIR,

XRD, XRF and FE-SEM. Renewable Energy, 2022, 183: 729-751.

Kang, J., Zhu, J., Wang, Y., et al. Dynamical modeling of coupled heat and mass transfer process of coalbed methane desorption in porous coal matrix. International Journal of Heat and Mass Transfer, 2022, 183: 122212.

Karimi, M., Rodrigues, A. E., Silva, J. Designing a simple volumetric apparatus for measuring gas adsorption equilibria and kinetics of sorption. Application and validation for CO_2, CH_4 and N_2 adsorption in binder-free beads of 4A zeolite. Chemical Engineering Journal, 2021, 425: 130538.

Li, B., Zhang, J., Ding, Z., et al. A dynamic evolution model of coal permeability during enhanced coalbed methane recovery by N_2 injection: Experimental observations and numerical simulation. RSC Advances, 2021, 11(28): 17249-17258.

Li, J., Pan, J., Wang, X., et al. Potential effect of carbon dioxide injection on the functional groups of medium volatile bituminous coals analysed using in-situ diffuse reflectance Fourier-transform infrared spectroscopy. International Journal of Coal Geology, 2023, 265: 104169.

Li, S., Qin, Y., Tang, D., et al. A comprehensive review of deep coalbed methane and recent developments in China. International Journal of Coal Geology, 2023, 279: 104369.

Li, Z., Elsworth, D. Controls of CO_2-N_2 gas flood ratios on enhanced shale gas recovery and ultimate CO_2 sequestration. Journal of Petroleum Science and Engineering, 2019, 179: 1037-1045.

Liao, Q., Zhou, J., Xian, X., et al. Competition adsorption of CO_2/CH_4 in shale: Implications for CO_2 sequestration with enhanced gas recovery. Fuel, 2023, 339: 127400.

Liu, J., Chen, Z., Elsworth, D., et al. Interactions of multiple processes during cbm extraction: A critical review. International Journal of Coal Geology, 2011, 87(3-4): 175-189.

Liu, Y., Wilcox, J. Effects of surface heterogeneity on the adsorption of CO_2 in microporous carbons. Environmental Science & Technology, 2012, 46(3): 1940-1947.

Long, H., Lin, H., Yan, M., et al. Molecular simulation of the competitive adsorption characteristics of CH_4, CO_2, N_2, and multicomponent gases in coal. Powder Technology, 2021, 385: 348-356.

Lu, J., Wang, X., Li, H., et al. Molecular insights into the methane adsorption capacity of coal under microwave irradiation based on solid-state ^{13}C-NMR and XPS. Fuel, 2023, 339: 127484.

Mabuza, M., Premlall, K., Daramola, M. O. Modelling and thermodynamic properties of pure CO_2 and flue gas sorption data on south african coals using Langmuir, Freundlich, Temkin, and extended Langmuir isotherm models. International Journal of Coal Science & Technology, 2022, 9: 45.

Neyertz, S., Brown, D. Single-and mixed-gas sorption in large-scale molecular models of glassy bulk polymers. Competitive sorption of a binary CH_4/N_2 and a ternary CH_4/N_2/CO_2 mixture in a polyimide membrane. Journal of Membrane Science, 2020, 614: 118478.

Omotilewa, O. J., Panja, P., Vega-Ortiz, C., et al. Evaluation of enhanced coalbed methane recovery and carbon dioxide sequestration potential in high volatile bituminous coal. Journal of Natural Gas Science and Engineering, 2021, 91: 103979.

Oudinot, A. Y., Koperna, G. J., Philip, Z. G., et al. CO_2 injection performance in the Fruitland coal fairway, San Juan Basin: Results of a field pilot. SPE Journal, 2011, 16(4): 864-879.

Packham, R., Connell, L., Cinar, Y., et al. Observations from an enhanced gas recovery field trial for coal mine gas management. International Journal of Coal Geology, 2012, 100: 82-92.

Pan, J., Zhang, Z., Li, M., et al. Characteristics of multi-scale pore structure of coal and its influence on permeability. Natural Gas Industry B, 2019, 6(4): 357-365.

Phan, V., Quirico, E., Beck, P., et al. Infrared spectroscopy quantification of functional carbon groups in kerogens and coals: A calibration procedure. Spectrochimica Acta Part A: Molecular and Biomolecular Spectroscopy, 2021, 259: 119853.

Ping, A., Xia, W., Peng, Y., et al. Construction of bituminous coal vitrinite and inertinite molecular assisted by ^{13}C NMR, FTIR and XPS. Journal of Molecular Structure, 2020, 1222: 128959.

Qadir, S., Gu, Y., Ali, S., et al. A thermally stable isoquinoline based ultra-microporous metal-organic framework for CH_4 separation from coal mine methane. Chemical Engineering Journal, 2022, 428: 131136.

Rainone, F., D'Agostino, O., Erto, A., et al. Biogas upgrading by adsorption onto activated carbon and carbon molecular sieves: Experimental and modelling study in binary CO_2/CH_4 mixture. Journal of Environmental Chemical Engineering, 2021, 9(5): 106256.

Salmachi, A., Zeinijahromi, A., Algarni, M. S., et al. Experimental study of the impact of CO_2 injection on the pore structure of coal: A case study from the Bowen Basin, Australia. International Journal of Coal Geology, 2023, 275: 104314.

Sander, R., Connell, L. D., Camilleri, M., et al. CH_4, CO_2, N_2 diffusion in Bowen Basin (Australia) coal: Relationship between sorption kinetics of coal core and crushed coal particles. Journal of Natural Gas Science and Engineering, 2020, 81: 103468.

Serafin, J., Kielbasa, K., Michalkiewicz, B. The new tailored nanoporous carbons from the common polypody (polypodium vulgare): The role of textural properties for enhanced CO_2 adsorption. Chemical Engineering Journal, 2022, 429: 131751.

Shen, Z., Liu, Y., Lei, J., et al. Changes in the three-dimensional molecular structure of coal during methane adsorption induced swelling. Process Safety and Environmental Protection, 2023, 180: 56-66.

Skoczylas, N., Pajdak, A., Kudasik, M., et al. CH_4 and CO_2 sorption and diffusion carried out in various temperatures on hard coal samples of various degrees of coalification. Journal of Natural Gas Science and Engineering, 2020,

81: 103449.

Su, E., Liang, Y., Zou, Q., et al. Numerical analysis of permeability rebound and recovery during coalbed methane extraction: Implications for CO_2 injection methods. Process Safety and Environmental Protection, 2021, 149: 93-104.

Talapatra, A. A study on the carbon dioxide injection into coal seam aiming at enhancing coal bed methane (ECBM) recovery. Journal of Petroleum Exploration and Production Technology, 2020, 10(5): 1965-1981.

Talapatra, A., Halder, S., Chowdhury, A. I. Enhancing coal bed methane recovery: Using injection of nitrogen and carbon dioxide mixture. Petroleum Science and Technology, 2021, 39(2): 49-62.

Thomas, H., Chen, M. Insights into carbon dioxide sequestration into coal seams through coupled gas flow-adsorption-deformation modelling. Journal of Rock Mechanics and Geotechnical Engineering, 2024, 16(1): 26-40.

Tursunov, O., Suleimenova, B., Kuspangaliyeva, B., et al. Characterization of tar generated from the mixture of municipal solid waste and coal pyrolysis at 800°C. Energy Reports, 2020, 6: 147-152.

Ursueguía, D., Díaz, E., Ordóñez, S. Metal-Organic Frameworks (MOFs) as methane adsorbents: From storage to diluted coal mining streams concentration. Science of The Total Environment, 2021, 790: 148211.

Wang, J., Tian, L., Li, G., et al. Construction of vitrinite molecular structures based on ^{13}C NMR and FTIR analysis: Fundamental insight into coal thermoplastic properties. Fuel, 2021, 300: 120981.

Wang, K., Pan, J., Xu, R., et al. Macromolecular rearrangement caused by CO_2 adsorption in coal. Fuel, 2023, 349: 128630.

Wang, K., Pan, J., Wang, E., et al. Potential impact of CO_2 injection into coal matrix in molecular terms. Chemical Engineering Journal, 2020, 401: 126071.

Wang, Z., Fu, X., Pan, J., et al. Effect of N_2/CO_2 injection and alternate injection on volume swelling/shrinkage strain of coal. Energy, 2023, 275: 127377.

Wei, G., Wen, H., Deng, J., et al. Liquid CO_2 injection to enhance coalbed methane recovery: An experiment and in-situ application test. Fuel, 2021, 284: 119043.

Wu, S., Deng, C., Wang, X. Molecular simulation of flue gas and CH_4 competitive adsorption in dry and wet coal. Journal of Natural Gas Science and Engineering, 2019, 71: 102980.

Xu, F., Yan, X., Wang, F., et al. Development strategy and countermeasures of China's CBM industry under the goal of "carbon peak and neutrality". Journal of Earth Science, 2023, 34(4): 975-984.

Yang, H., Xiong, Y., Xie, Z., et al. Quantitative characterization of coal structure by high-resolution CP/MAS ^{13}C solid-state NMR spectroscopy. Proceedings of the Combustion Institute, 2021, 38(3): 4161-4170.

Yasemi, S., Khalili, Y., Sanati, A., et al. Carbon capture and storage: Application in the oil and gas industry. Sustainability, 2023, 15(19): 14486.

Zhang, L., Ye, Z., Li, M., et al. The binary gas sorption in the bituminous coal of the Huaibei Coalfield in China. Adsorption Science & Technology, 2018, 36(9-10): 1612-1628.

Zhang, X., Lu, X., Xiao, M., et al. Molecular reaction dynamics simulation of pyrolysis mechanism of typical bituminous coal via ReaxFF. Journal of Fuel Chemistry and Technology, 2020, 48(9): 1035-1046.